# Quantifying macro- and microscale alignment of carbon microfibers in polymer-matrix composite materials fabricated using ultrasound directed self-assembly and 3D-printing

K. Niendorf, B. Raeymaekers*

*Department of Mechanical Engineering, University of Utah, Salt Lake City, UT 84112, USA*

ABSTRACT

Aligning microfibers along a user-specified direction is important to fabricate polymer-matrix composite materials with tailored properties, including anisotropic electrical and thermal conductivity and high strength-to-weight ratio. Building on our earlier work, we employ ultrasound directed self-assembly to align carbon microfibers along user-specified directions in photopolymer resin and use stereolithography to cure the resin and 3D print composite materials. We quantify macro- and microscale alignment of microfibers in the matrix as a function of weight fraction and dimensionless ultrasound transducer separation distance and input power. Multiple regression analysis expresses microfiber alignment as a function of the fabrication process parameters and shows that microscale alignment is primarily determined by microfiber weight fraction, whereas macroscale alignment is a function of microfiber weight fraction, dimensionless ultrasound transducer separation distance and input power. Relating microfiber alignment to the fabrication process parameters is a crucial step towards 3D-printing polymer-matrix composite materials with tailored material properties.

## 1. Introduction

Polymer-matrix micro- and nanofiber-reinforced composite materials consist of a polymer matrix material and a fiber filler material. These composite materials receive considerable interest in the scientific community due to potential applications as low-density materials with multi-functional and tailored properties. Examples include anisotropic thermal [1] and electrical [2] conductivity, electromagnetic shielding [3,4], and structural reinforcement [5,6]. The composite material properties depend on the matrix and the fiber filler material properties, the interaction between both constituents, and the filler material arrangement in the matrix.

Integrating fibers in the polymer matrix material occurs in two ways. One can spin nanofibers into long continuous fibers and embed them in the polymer matrix [7] or disperse micro- or nanofibers directly into the polymer matrix material to obtain discontinuous reinforcement [8]. In the latter case, the micro- or nanofibers orient in random directions [9] or arrange in specific patterns or alignment tailored to the desired properties and functionality of the composite material [10]. The properties of the composite material are determined primarily by dispersion of the fibers in the polymer matrix [11], the adhesion or interfacial bonding between the micro- or nanofibers and the polymer matrix [12], and the alignment of the micro- or nanofibers in the polymer matrix [13]. In this work, we specifically focus on fiber alignment. For instance, it is well-known that aligning nano- or microfibers enhances electrical [14] and thermal [15] conductivity of polymer-matrix fiber-reinforced composite materials by reducing the percolation threshold [16], and also increases tensile strength [17], modulus of elasticity [2], and fracture toughness [18].

Several methods exist to directly align micro- or nanofibers in a polymer matrix material using external fields, including electric [19], magnetic [20], shear/flow [21], and ultrasound fields [22,23]. Shear and flow fields both rely on shear forces to orient fibers and have been used in both liquid and solid specimens. Electric and magnetic fields orient fibers into user-specified directions [24,25], but require ultra-high field strengths [26,27], which limits dimensional scalability. Additionally, the fibers must be electrically conductive or ferromagnetic, respectively, which limits material choice. In contrast, ultrasound wave fields show low attenuation in low-viscosity fluids [28], and the acoustic radiation force associated with an ultrasound wave allows manipulating particles independent of material properties [29] or shape [30]. Our research group has previously demonstrated ultrasound directed self-assembly (DSA) in combination with stereolithography (SLA) to align carbon microfibers in liquid photopolymer resin before

curing a polymer composite material specimen using UV light [31].

Quantifying microfiber alignment as a function of the fabrication process parameters is crucial to link the fabrication process to the resulting physical properties of the composite material. Macroscale alignment of clusters of microfibers describes the bulk structure of the composite material, whereas measuring microscale alignment yields information about the orientation of individual microfibers in the polymer matrix. Both macro- and microscale alignment, and the relationship between them, contribute to the properties of the composite material.

Thus, several methods exist to quantify the alignment of microfibers in composite materials. Tensile testing determines the mechanical properties of a material specimen, which relates to the alignment of its fiber reinforcement [33,43], but only yields information about bulk, not individual alignment of the microfibers. Scholz et al. ultrasonically aligned clusters of glass microfibers in various thermoset resins and quantified alignment using mechanical testing, by measuring the effect of aligning microfibers on several material properties and making qualitative observations of microfiber weight fraction and alignment [32]. Another method relies on digital image processing to compute a fiber orientation factor, which quantifies the alignment between individual microfibers and a specified axis [33]. However, individual microfibers must be manually identified in microscopy images, which introduces the possibility of bias and error. Haslam and Raeymaekers aligned clusters of carbon nanotubes (CNTs) using ultrasound DSA in two-part urethane resin and measured a difference between the user-specified and the mean CNT alignment angle of less than 5.1° [33]. Measuring electrical conductivity of a composite material also quantifies microfiber alignment [34], but requires the microfibers to be electrically conductive and form a percolated network through the specimen, and it only provides information about bulk alignment, without measuring microfiber-specific information. Raman spectroscopy quantifies microfiber alignment by comparing the intensity of the Raman spectra between specimens [35] but does not indicate the alignment angles or collect any microfiber-specific information. Chapkin et al. used an electric field to align CNTs in epoxy resin [35,36]. They quantified alignment using Raman spectroscopy and found increasing CNT alignment with increasing field strength. Alternatively, measuring anisotropy using the fast Fourier transform (FFT) provides information about the primary alignment directions and how well individual microfibers align with these directions [37].

No papers exist in the literature that relate the alignment of microfibers to the process parameters of ultrasound DSA, combined with 3D-printing. Additionally, no published works connect macro- and microscale alignment of microfibers aligned with external fields, or with ultrasound DSA specifically. However, this information is crucial to using ultrasound DSA as a fabrication method for polymer-matrix microfiber-reinforced composite materials and multifunctional engineered materials. Thus, the objective of this paper is to quantify and correlate the macro- and microscale alignment of carbon microfibers embedded in photopolymer resin, resulting from the combined ultrasound DSA and SLA 3D-printing process parameters.

## 2. Methods and materials

### 2.1. 3D-printing composite material specimens

Fig. 1 schematically shows the experimental setup we use to fabricate polymer-matrix microfiber-reinforced composite material specimens with discontinuous lines of aligned carbon microfibers, implementing the combined ultrasound DSA and SLA 3D-printing process previously demonstrated by our research group [31]. Fig. 1 (a) shows a 30.4 × 30.0 × 6.0 mm reservoir that contains a mixture of photopolymer resin with dynamic viscosity $\mu$ (viscosity 90 cP, density 1.1 g/cc, Makerjuice G+) with a pre-defined weight fraction of carbon microfibers $w_f$ (diameter 7.2 μm, length 100 μm, density 1.75 g/cc, Zoltek

PX30 MF150) dispersed in it (sonicator Hielscher UP200Ht, power 35.0 W, time 5 min). Two ultrasound transducers (PZT type SM111, center frequency $f_c$ = 1.5 MHz) are affixed to opposing reservoir walls and separated by a distance $d$, and create a standing ultrasound wave in the photopolymer/microfiber mixture using a radio-frequency (RF) amplifier (E&I 2100L) and a function generator (Tektronix AFG 3102). The acoustic radiation force associated with the ultrasound wave field drives the carbon microfibers to the nodes of the ultrasound standing wave, spaced a half-wavelength apart, where they align with each other and the node [38–40] (Fig. 1(b)). Fig. 1(c) depicts curing the photopolymer with UV light exposure (data projector ViewSonic PJD7822HDL), which fixates the aligned microfibers in place. We evacuate the cured material specimen from the reservoir and evaluate the alignment of the microfibers. Fig. 1 (d) shows a typical 10.00 × 5.00 × 0.75 mm composite material specimen that results from the 3D-printing process illustrated in Fig. 1(a–c), and depicts the discontinuous lines of aligned microfibers embedded in the cured photopolymer resin. See Table S1 in the supplemental information for specific 3D-printing process parameters.

### 2.2. Identifying dimensionless parameters

We use the Buckingham Pi theorem [41] to reduce the number of independent parameters that describe the ultrasound DSA process to align microfibers in photopolymer resin: ultrasound transducer separation distance $d$, voltage $V$, impedance $Z$, ultrasound exposure time $t$, dynamic viscosity of the photopolymer resin $\mu$, microfiber weight fraction $w_f$, and wavelength $\lambda = c/f$, with the sound propagation velocity in the photopolymer resin medium $c$ = 1364 m/s (measured using a pulse-echo experiment), and the operating frequency of the ultrasound transducers $f$, which is close to their center frequency of 1.5 MHz. The dependent parameter is the alignment angle $\theta$ of a cluster of microfibers (macroscale alignment) or individual microfibers (microscale alignment). Buckingham Pi analysis results in four dimensionless parameters; the first and second dimensionless parameters are the microfiber alignment angle $\theta$ and the microfiber weight fraction $w_f$. The third dimensionless parameter represents a dimensionless input power to the ultrasound transducers, $P = |V|^2 t^2/(\mu \lambda^3 \text{Re}(Z))$, which is the real part of the input power per unit fluid volume. Note that Re($Z$) refers to the real part of the impedance $Z$. The fourth dimensionless parameter is the separation between the ultrasound transducers $D = d/\lambda$. We experimentally quantify the microfiber alignment angle as a function of the other three dimensionless parameters, i.e., $\theta = f(w_f, P, D)$, using a full factorial experiment with three discrete treatment levels for each of the three independent dimensionless parameters. Table 1 summarizes the treatment levels we use in this work. The significant digits represent the true experimental accuracy of each parameter.

Based on trial measurements of the microfiber alignment (orientation angle arithmetic mean and standard deviation) we compute that a minimum of five specimen replications are required to obtain statistically significant microfiber alignment measurements, considering a statistical power of 80% with a 95% confidence interval. Thus, we 3D-print a total of 135 composite material specimens with aligned microfibers: five specimen replications for each of the 27 possible combinations of dimensionless parameter treatment levels.

We identify treatment limits of each dimensionless parameter such that they represent extreme values for our 3D-printing and alignment quantification process. We choose the microfiber weight fraction treatment levels in terms of practical considerations; $w_f < 0.1$ is difficult to observe visually, whereas $w_f > 0.5$ results in microfiber clusters that are too dense to easily identify individual microfibers. We vary the treatment level of $P$ using the input voltage $V$ to the ultrasound transducers (30.5–51.6 V), where we choose the lowest voltage as the minimum voltage that results in visual alignment of the microfibers, and the voltage higher than the highest voltage level causes boiling of the photopolymer resin. Finally, we vary $D$ from $18.0 \leq D \leq 36.0$ by
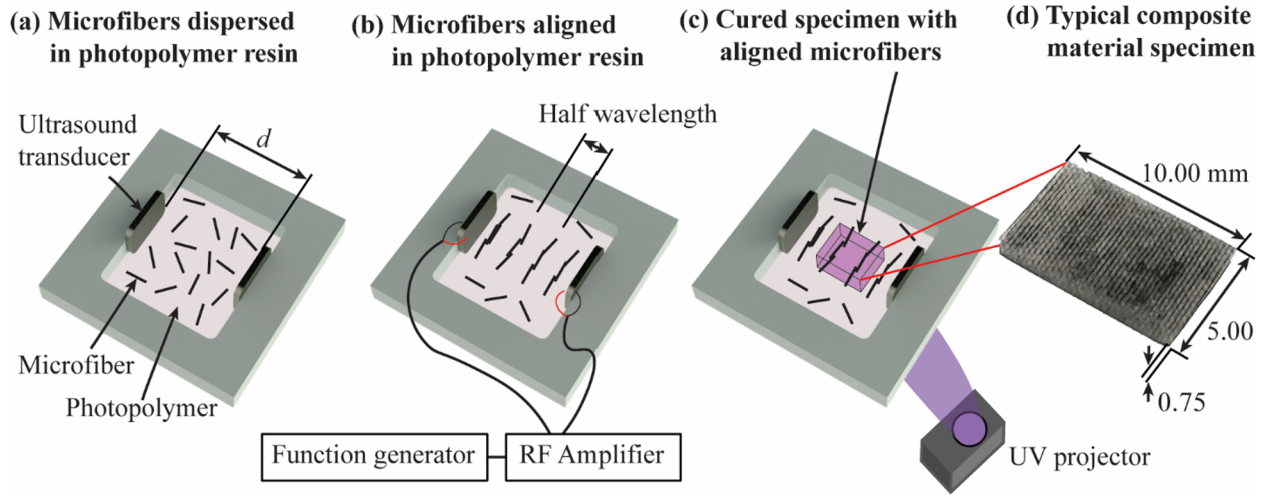
**Fig. 1.** (a) Reservoir that contains photopolymer resin with dispersed microfibers. (b) Ultrasound transducers create a standing ultrasound wave in the reservoir, driving the microfibers to the nodes of the wave. (c) UV exposure cures the photopolymer resin and fixates the aligned microfibers in place. (d) Picture of a typical composite material specimen resulting from this 3D-printing process, showing the aligned microfibers as dark lines within the light-colored photopolymer resin. (For interpretation of the references to colour in this figure legend, the reader is referred to the web version of this article.)

**Table 1**
Treatment levels for dimensionless parameters in the factorial study.

| Independent dimensionless parameter | Treatment 1 | Treatment 2 | Treatment 3 |
| --- | --- | --- | --- |
| Microfiber weight fraction, $w_f$ | 0.1 | 0.3 | 0.5 |
| Input power, $P$ | 2.85e+13 | 4.44e+13 | 6.02e+13 |
| Ultrasound transducer separation distance, $D$ | 18.0 | 27.0 | 36.0 |

altering the reservoir dimensions and fine-tuning $f$ such that $D$ is an integer multiple of the wavelength. We choose these limits to fit a 10.0 mm specimen in the reservoir and avoiding significant ultrasound wave attenuation when $D$ is large.

### 2.3. Image processing and analysis

We sand and polish the specimens using silicon carbide polishing paper up to 1200 grit to ensure consistent surface quality. We use an optical microscope (Keyence VHX-5000) to capture $100\times$ and $500\times$ magnification images of each specimen, to determine the microfiber alignment at the macro- and microscale, respectively. Fig. 2 shows a typical composite material specimen after surface preparation. We choose the imaging locations to determine the microfiber alignment in the specimen as follows: we select a 2.47-by-2.47 mm area to identify macroscale alignment (red square in Fig. 2). The microscale alignment may vary within the area in which we quantify the macroscale alignment due to imperfections in the acoustic field (misalignment of transducers, reflections) or non-uniform microfiber dispersion. Therefore, we select five 650-by-650 μm areas (blue squares in Fig. 2), located as shown in Fig. 2, to measure microscale alignment, and we average the microscale alignment measurement over these five locations. The size of the area for macro- and microscale microfiber alignment measurement and the number of locations of microscale microfiber alignment measurement follow from convergence studies.

We enhance the brightness of the macro- and microscale images to maximize the contrast between photopolymer resin and microfibers, and convert each image to a binary image. We employ a two-dimensional FFT to quantify the anisotropy in each binary image [37]. The FFT anisotropy $\Phi$ represents a distribution of the alignment angles $\theta$ of clusters of microfibers (macroscale alignment measurement) or

individual microfibers (microscale alignment measurement) present in the binary image. After normalizing, the integral of $\Phi$ between $-\pi/2 \le \theta \le \pi/2$ has unit magnitude, and $\Phi = f(\theta)$ is the probability density function (PDF) of the alignment angle $\theta$. We quantify microfiber alignment as the probability of a cluster of microfibers (macroscale alignment measurement), or an individual microfiber (microscale alignment measurement) orienting within $\pm \Delta\theta°$ of the user-specified alignment angle $\theta_s = 0°$. Fig. 3 shows the sequence of (a) obtaining an optical image (e.g., $500\times$ to quantify microscale alignment), (b) converting the optical image to a binary image, and (c) computing the FFT anisotropy $\Phi(\theta)$ of the binary image. Integrating $\Phi(\theta)$ between $\pm \Delta\theta°$ yields the probability $p_a$ that the alignment of a randomly selected individual microfiber or cluster of fibers in the image orients within the user-specified alignment angle $\pm \Delta\theta°$, i.e.,

$$p_a = \int_{-\Delta\theta}^{\Delta\theta} \phi(\theta)d\theta \tag{1}$$

We choose $\Delta\theta° = 10°$ because it leads to a normally distributed alignment probability $p_a$ for both macro- and microscale alignment measurement datasets, which is a requirement for parametric regression analysis. We compute $p_a$ for both the macro- and microscale alignment measurement datasets obtained from all 135 composite material specimens we fabricate. Multiple regression analysis on the two separate datasets, with the three independent dimensionless input parameters $w_f$, $P$, and $D$, and the dependent dimensionless output parameter $p_a$, reveals which dimensionless input parameters have a statistically significant effect on the dependent output parameter. We consider a $p$-value $\le 0.05$ statistically significant but also report the actual $p$-value. If two effects are collinear, we remove the higher-order term in the regression model because including collinear effects can cause misleading regression
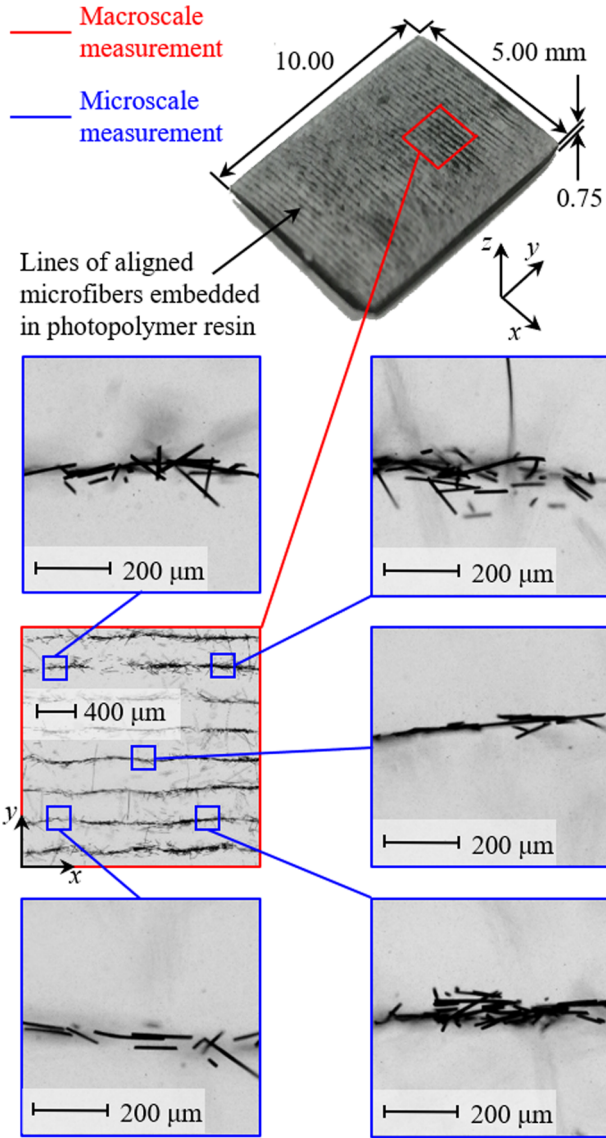
**Fig. 2.** Typical composite material specimen after surface preparation, with inset images that illustrate the locations for macro- and microscale microfiber alignment measurement. (For interpretation of the references to colour in this figure legend, the reader is referred to the web version of this article.)

coefficients and *p*-values [42]. We identify the best multiple regression model by comparing the root-mean-square error of logarithmic, exponential, square root, inverse, and polynomial fits.
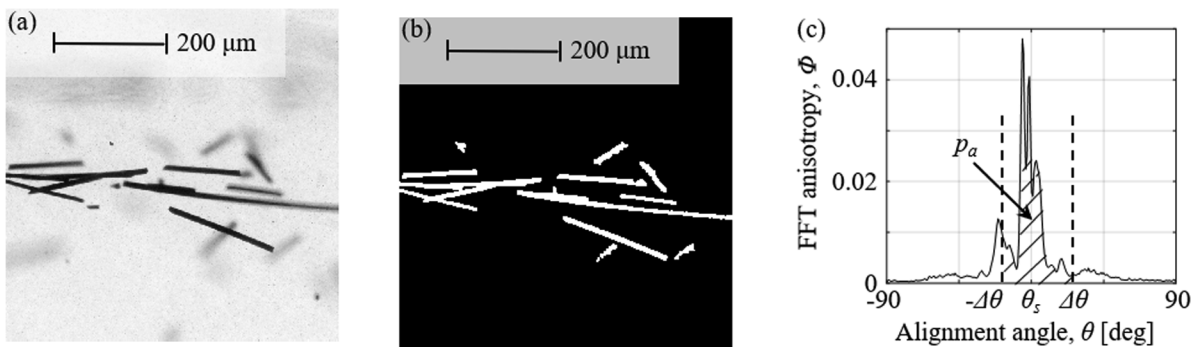
## 3. Results and discussion

Fig. 4 shows the macro- (left column) and microscale (right column) alignment probability $p_a$ as a function of the three dimensionless parameters $w_f$ (Fig. 4(a) and (b)), $P$ (Fig. 4(c) and (d)), and $D$ (Fig. 4(e) and (f)). We identify different treatment levels of each dimensionless parameter with colored lines and markers (see legend of Fig. 4). Each data point represents the average of five different composite material specimens, whereas the error bars show one standard deviation. The alignment probability ranges from 0.22 to 0.57, where 0.22 indicates poor alignment and 0.57 indicates excellent alignment.

Fig. 5 shows images of six specimens that illustrate the physical effect of each independent dimensionless input parameter on the microfiber alignment to further explain the results of Fig. 4. Fig. 5(a) and (b) show increasing $w_f$ with constant $P$ and $D$, Fig. 5(c) and (d) show increasing $P$ with constant $w_f$ and $D$, and Fig. 5(e) and (f) show increasing $D$ with constant $w_f$ and $P$. For each specimen, we show an image of the macroscale microfiber alignment with an inset image of the microscale microfiber alignment. Furthermore, we perform multiple regression analysis on the macro- and microscale microfiber alignment measurement datasets and Eqs. (2 and 3) show the best predictor models (based on RMS error macro: 0.0813, micro: 0.0739), respectively.
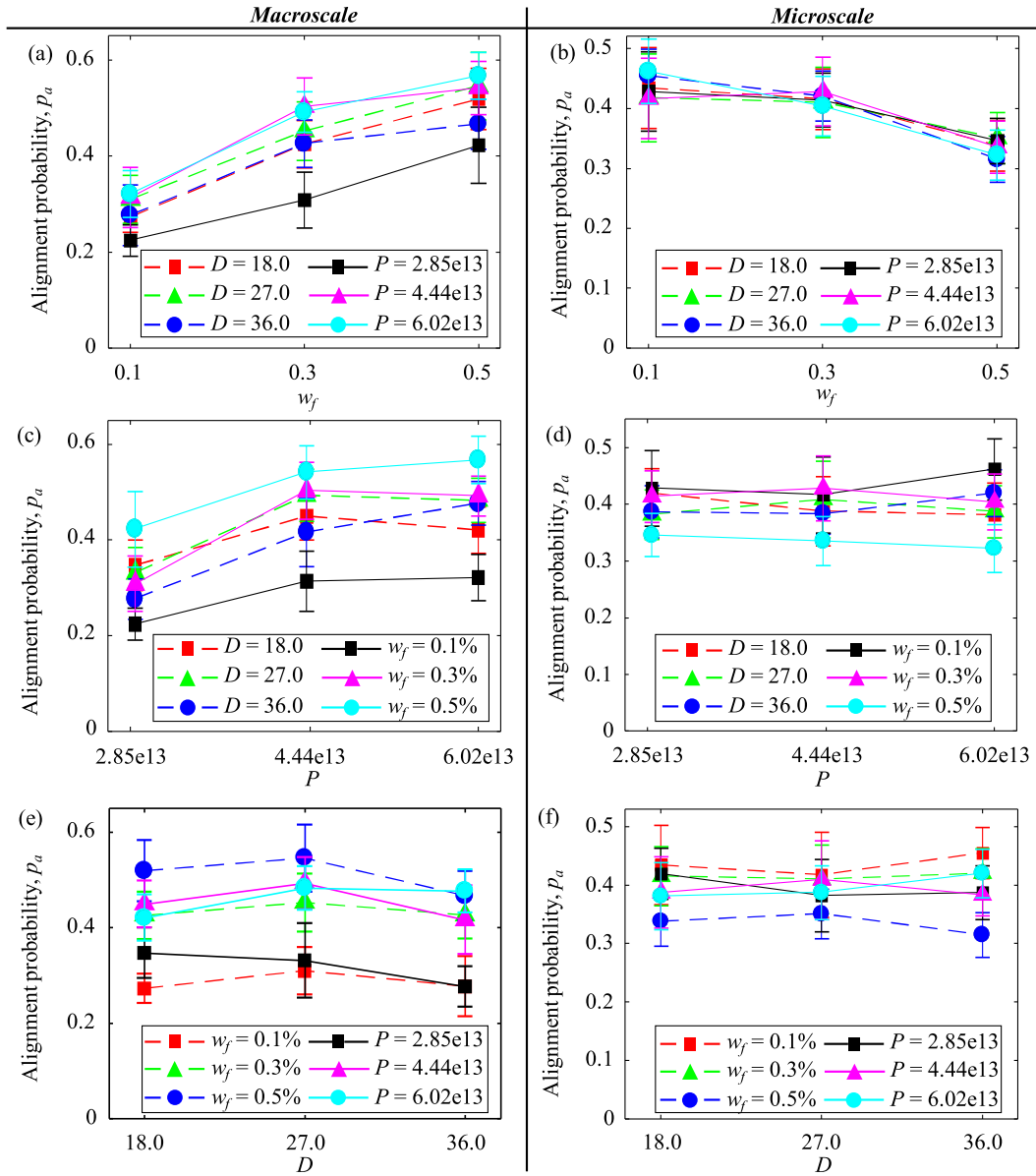
$$p_a = -0.523 + 1.13w_f - 0.843w_f^2 + (2.04 * 10^{-28})P - (2.60 * 10^{-28})P^2 + 0.0172D - (4.74 * 10^{-4})D^2 + (3.77 * 10^{-15})w_f P - (8.93 * 10^{-3})w_f D + (2.22 * 10^{-16})DP$$

(2)

$$p_a = 0.812 - 0.187e^{w_f} - (3.61 * 10^{-15})P - (6.07 * 10^{-3})D + (1.36 * 10^{-16})DP$$

(3)

All regression terms, whether statistically significant or not, are included in Eqs. (2) ($R^2 = 0.679$) and (3) ($R^2 = 0.263$) because we assume they all influence microfiber alignment. Tables 2 and 3 show the *p*-values for each of the terms in the multiple regression analysis of the macro- and microscale alignment datasets, respectively, where e.g. $w_f$:$P$ indicates the interaction effect between $w_f$ and $P$.

Combining the macro- and microscale alignment probability results of Fig. 4, images of microfiber alignment of composite material specimens 3D-printed with different dimensionless input parameter treatment levels shown in Fig. 5, the multiple regression analysis resulting in Eqs. (2 and 3), and their corresponding *p*-values shown in Tables 2 and 3, allow identifying the contribution of each dimensionless parameter to the macro- and microscale alignment probability, respectively.

Fig. 4(a) shows the macroscale alignment probability $p_a$ as a function of microfiber weight fraction $w_f$ for three treatment levels of both $P$ and $D$. We observe that $p_a$ increases with increasing $w_f$ for all treatments of $P$ and $D$. Increasing $w_f$ increases the number of microfibers that accumulate at the nodes of the ultrasound standing wave, thus increasing the density of microfibers at the nodes. The presence of an increased



**Fig. 3.** (a) Optical image at 500× magnification. (b) Binary conversion of (a). (c) FFT anisotropy Φ(θ) of the binary image. The hatched area corresponds to the probability that a randomly selected cluster of microfibers (macroscale alignment measurement) or individual microfiber (microscale alignment measurement) is aligned within ± Δθ° of the user-specified alignment angle θ$_s$ = 0°.

**Fig. 4.** Macro- and microscale alignment probability $p_a$ as a function of each dimensionless parameter: (a–b) $p_a(w_f)$, (c–d) $p_a(P)$, and (e–f) $p_a(D)$. (For interpretation of the references to colour in this figure legend, the reader is referred to the web version of this article.)

number of microfibers at the nodes of the standing ultrasound wave physically forces the microfiber clusters to align, which is evident from comparing Fig. 5(a) and (b). Fig. 4(b) shows the microscale alignment probability that corresponds to Fig. 4(a). We observe that for all treatments of $P$ and $D$, $p_a$ decreases with increasing $w_f$ because the microfibers increasingly entangle with increasing $w_f$. As a result, the entanglement prevents the individual microfibers to freely rotate and align with the nodes of the standing ultrasound wave, which is evident from comparing the inset images of Fig. 5(a) and (b).

Fig. 4(c) shows the macroscale alignment probability $p_a$ as a function of dimensionless input power $P$ for three treatment levels of both $w_f$ and $D$. We observe that $p_a$ increases with increasing $P$ for all treatment levels of $w_f$ and $D$, because the acoustic radiation force that the microfibers experience increases with increasing $P$. Thus, increasing the acoustic radiation force increases the number of microfibers that align with the nodes of the ultrasound standing wave, which we observe by comparing Fig. 5(c) and (d). Increasing $P$ also counteracts ultrasound wave attenuation in the photopolymer resin, but ultimately leads to boiling and streaming of the photopolymer resin because the input

power converts to heat that cannot be dissipated fast enough from the reservoir. Fig. 4(d) shows the microscale alignment probability that corresponds to Fig. 4(c). Qualitative observations of the inset images of Fig. 5(c) and (d) and regression $p$-values > 0.05 in Table 3 show that $P$ does not significantly affect $p_a$ at the microscale. $w_f$ is high, and the microfibers entangle, preventing increased $P$ from affecting the microscale microfiber alignment.

Fig. 4(e) shows macroscale alignment probability $p_a$ as a function of dimensionless ultrasound transducer separation distance $D$ for all three treatment levels of both $w_f$ and $P$. We observe that $p_a$ decreases with increasing $D$, because the attenuation of the ultrasound wave in the photopolymer resin increases with increasing $D$, and in turn decreases the magnitude of the acoustic radiation force acting on the microfibers. Thus, fewer microfibers align at the nodes of the ultrasound standing wave, which we observe by comparing Fig. 5(e) and (f). Although this trend is not necessarily visually apparent in Fig. 4(e), regression analysis confirms that it is statistically significant. Fig. 4(f) shows the microscale alignment probability that corresponds to Fig. 4(e). Qualitative observations of the inset images of Fig. 5(e) and (f) and regression $p$-
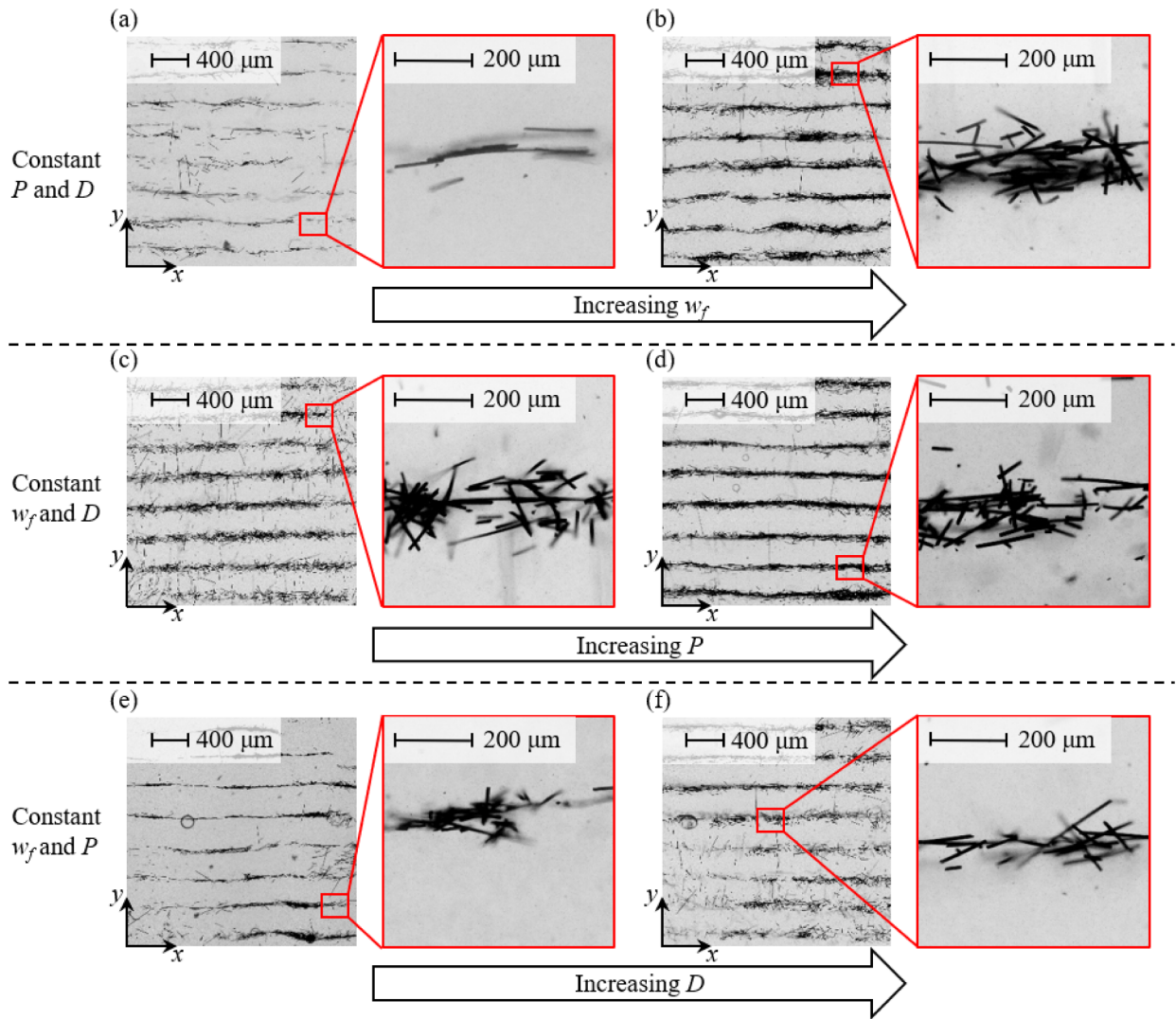
**Fig. 5.** Illustration of the physical effects underlying the microfiber alignment results of Fig. 4. (a–b) increasing $w_f$ with constant $P$ and $D$, (b–c) increasing $P$ with constant $w_f$ and $D$, (e–f) increasing $D$ with constant $w_f$ and $P$. (For interpretation of the references to colour in this figure legend, the reader is referred to the web version of this article.)

**Table 2**
Regression $p$-values of macroscale alignment probability.

| Regression effect | $w_f$ | $w_f^2$ | $P$ | $P^2$ | $D$ | $D^2$ | $w_f{:}P$ | $w_f{:}D$ | $D{:}P$ |
|---|---|---|---|---|---|---|---|---|---|
| $p$-value | 7.97E−4 | 0.0339 | 9.10E−4 | 5.37E−5 | 0.122 | 0.0148 | 0.276 | 0.173 | 5.16E−3 |

values $> 0.05$ in Table 3 show that $D$ does not significantly affect $p_a$ at the microscale. We note that in Fig. 4(e) the lines of constant $P$ cross, revealing an interaction between $P$ and $D$ in terms of macroscale microfiber alignment; we increase $P$ to counteract decreasing acoustic radiation force acting on the microfibers when the ultrasound wave attenuation increases with increasing $D$. The significance of the interaction effect between $P$ and $D$ implies that dimensional scalability of ultrasound DSA is possible by tuning $P$ and $D$.

From Table 2 and 3, we observe that the independent dimensionless

**Table 3**
Regression $p$-values of microscale alignment probability.

| Regression effect | $\exp(w_f)$ | $P$ | $D$ | $D{:}P$ |
|---|---|---|---|---|
| $p$-value | 2.92E−9 | 0.0669 | 0.0657 | 0.0572 |

parameters derived from the ultrasound DSA fabrication process affect macro- and microscale alignment probability $p_a$ differently. $w_f$ dominates $p_a$ at both the macro- and microscale but in opposite ways; once microfibers accumulate at the nodes of the ultrasound standing wave, adding additional microfibers causes the microfiber clusters to increase in size, which increases macroscale $p_a$, while the individual microfibers become more entangled, reducing microscale $p_a$. $P$ and $D$ are significant at the macroscale, but not at the microscale. Microfiber clusters change in size in response to changing $P$ or $D$, independent of $w_f$. However, once microfibers accumulate at the nodes of the standing ultrasound wave, they entangle, and changing $P$ or $D$ does not significantly change $p_a$ at the microscale.

Fig. 6 shows images of three specimens with different combinations of macro- and microscale microfiber alignment probability, which illustrate how changing the dimensionless ultrasound DSA process parameters affect alignment probability across multiple scales.
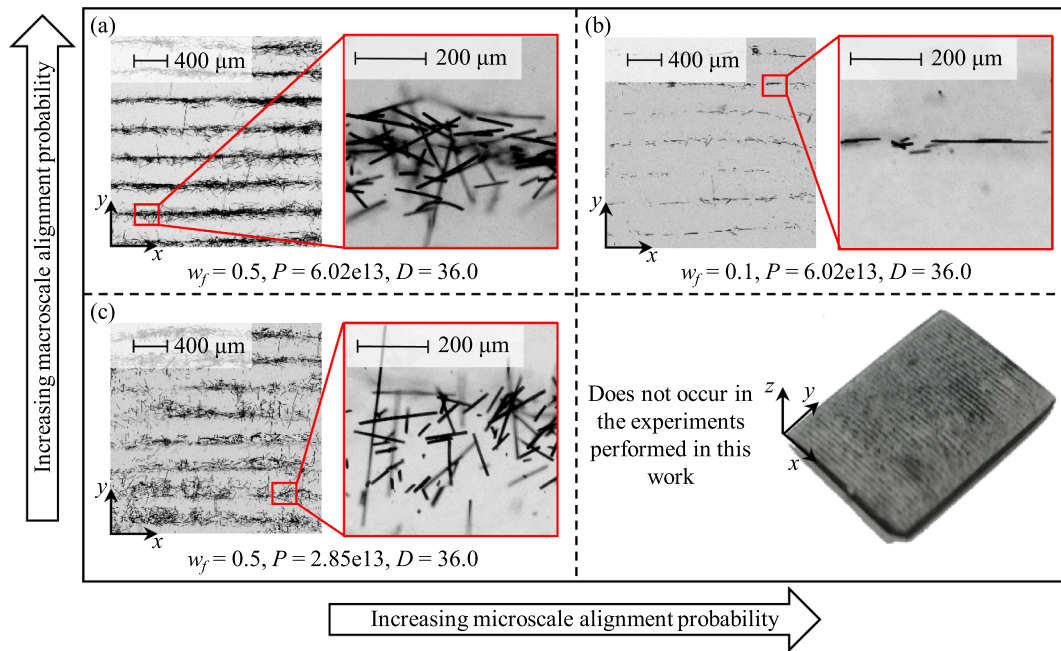
**Fig. 6.** Three extreme combinations of macro- and microscale alignment probability: (a) highly aligned microfiber clusters at the macroscale and not-well-aligned individual microfibers at the microscale, (b) highly aligned microfibers at both the macro- and microscale, (c) not-well-aligned microfibers at both the macro- and microscale. (For interpretation of the references to colour in this figure legend, the reader is referred to the web version of this article.)

Fig. 6(a) shows highly aligned clusters of microfibers at the macroscale, contrasting the not-well-aligned individual microfibers at the microscale. The high $P$ counteracts attenuation of the ultrasound wave from the large $D$, organizing thick lines of aligned microfiber clusters at the nodes of the ultrasound standing wave, while the microfibers entangle with each other due to the high $w_f$. Fig. 6(b) shows highly aligned microfibers at both the macro- and microscale. High $P$ counteracts ultrasound attenuation from a large $D$, and the $w_f$ is low such that microfibers do not entangle and can freely rotate to align parallel to the nodes of the ultrasound standing wave. Fig. 6(c) shows microfibers with low alignment at both the macro- and microscale. $P$ is not sufficiently high to counteract ultrasound attenuation, and high $w_f$ causes the microfibers to entangle. Finally, we do not observe any composite material specimens in the experiments conducted for this work that display low macroscale $p_a$ and high microscale $p_a$. If the ultrasound radiation force is not strong enough to drive the microfibers to the nodes of the ultrasound standing wave, the microfibers will not align parallel to the nodes at any scale.

Although no work in the open literature comprehensively relates microfiber alignment to the ultrasound DSA process parameters, several papers identify relationships between individual fabrication parameters and alignment. Scholz et al. align glass microfibers in epoxy using ultrasound directed self-assembly [32], and they observe that composite material specimens with low $w_f$ of glass microfibers have distinct features at the macroscale and well-aligned microstructures. They also observe that increasing $w_f$ results in longer and denser lines of aligned glass microfibers at the macroscale, with misaligned microstructures. These observations are consistent with our findings. For instance, $w_f$ is higher in Fig. 6(a) than in (b), with all other parameters constant. We observe that Fig. 6(b) shows distinct thin lines of aligned microfibers at the macro- and microscale, while the high $w_f$ of Fig. 6(a) results in dense lines of entangled microfibers. Furthermore, Chapkin et al. use an alternating current electric field to align CNTs in epoxy resin [35,36]. They observe increasing CNT alignment with increasing field strength, which is in line with the results documented in this work. For instance, the specimens shown in Fig. 6(a) and (c) differ only by $P$, which is proportional to the ultrasound field strength. $P$ in Fig. 6(a) is higher than that in (c) and results in increased macroscale alignment. Haslam

and Raeymaekers align CNTs in low-viscosity urethane resin using ultrasound directed self-assembly [33]. They find that macroscale CNT alignment decreases with increasing $w_f$, which contrasts the observation in this work. One explanation is that Haslam and Raeymaekers use CNTs instead of microfibers, which entangle more as a result of their higher aspect ratio and surface area to volume ratio. Also, the significantly higher $w_f$ in [33] than in this study could result in a CNT density at the nodes of the ultrasound wave field that is much higher than that in this work and, therefore, reduce CNT alignment.

The $R^2$ values of the macro- and microscale alignment probability predictor models suggest that the ultrasound DSA process has variability unexplained by the alignment probability predictor models, due to either natural process variation or a process parameter not included in the study. Further investigation of the $R^2$ values shows that the specimen replication standard deviation is as high as 23% of the average $p_a$ at the macroscale and 16% at the microscale, confirming that ultrasound DSA has high natural process variance. Even though the quantitative analysis displays high process variance, the qualitative interpretation of the results substantiates the physical mechanisms.

Our study of the ultrasound DSA process has several limitations. We only evaluate one type of microfiber and photopolymer resin for practical purposes, and thus do not account for different physical properties of microfibers and photopolymer resin during dimensional analysis. Also, our 3D-printing technique only allows fabrication of thin composite materials, which prohibits microfiber alignment in the thickness direction. Therefore, we verify that microfiber alignment is consistent through the thickness of a specimen, which we have shown for some of the specimens (see Figure S2 in the supplemental information). However, the results are based on a single cross-section in each specimen. Additionally, measuring alignment using a 2D FFT breaks down when microfibers are vertically embedded in the photopolymer resin, which limits the application of our alignment quantification method to composite materials with in-plane fibers.

Characterizing microfiber alignment as a function of the ultrasound DSA process parameters is an essential step towards developing multifunctional materials with properties tailored to specific applications. For example, once we understand how microfiber alignment relates to electrical conductivity, we can optimize the DSA process parameters to

create a 3D-printed part to achieve specific anisotropic electrical properties.

## 4. Conclusions

The alignment of microfibers embedded in photopolymer resin composite materials 3D-printed using ultrasound DSA and SLA depends on the scale of the analysis region; macroscale alignment does not indicate microscale alignment, and alignment at both scales must be considered independently. Microscale alignment is primarily driven by microfiber weight fraction only, whereas macroscale alignment is significantly affected by microfiber weight fraction, dimensionless ultrasound transducer input power, and dimensionless ultrasound transducer separation distance. Once microfibers accumulate at the nodes of the standing ultrasound wave, they entangle and prevent changes in dimensionless ultrasound transducer input power or separation distance from significantly affecting the alignment of individual microfibers. However, changing dimensionless input power or ultrasound transducer separation distance drives clusters of microfibers to change in size, independent of microfiber weight fraction. Thus, characterizing microfiber alignment as a function of the 3D-printing process parameters is a crucial step towards linking the process parameters to specific anisotropic material properties, such as electrical and thermal conductivity. This knowledge can be used in 3D-printing and rapid prototyping to optimize the fabrication of layered composite materials with patterns of embedded microfibers.

## Acknowledgment

## Appendix A. Supplementary material

Supplementary data to this article can be found online at https://doi.org/10.1016/j.compositesa.2019.105713.

## References

[1] Choi ES, Brooks JS, Eaton DL, Al-Haik MS, Hussaini MY, Garmestani H, et al. Enhancement of thermal and electrical properties of carbon nanotube polymer composites by magnetic field processing. J Appl Phys 2003;94:6034–9. https://doi.org/10.1063/1.1616638.

[2] Khan SU, Pothnis JR, Kim JK. Effects of carbon nanotube alignment on electrical and mechanical properties of epoxy nanocomposites. Compos Part A Appl Sci Manuf 2013;49:26–34. https://doi.org/10.1016/j.compositesa.2013.01.015.

[3] Liu Z, Bai G, Huang Y, Ma Y, Du F, Li F, et al. Reflection and absorption contributions to the electromagnetic interference shielding of single-walled carbon nanotube/polyurethane composites. Carbon NY 2007;45:821–7. https://doi.org/10.1016/j.carbon.2006.11.020.

[4] Yu WC, Wang T, Zhang GQ, Wang ZG, Yin HM, Yan DX, et al. Largely enhanced mechanical property of segregated carbon nanotube/poly(vinylidene fluoride) composites with high electromagnetic interference shielding performance. Compos Sci Technol 2018;167:260–7. https://doi.org/10.1016/j.compscitech.2018.08.013.

[5] Lau AK-T, Hui D. The revolutionary creation of new advanced materials—carbon nanotube composites. Compos Part B Eng 2002;33:263–77. https://doi.org/10.1016/S1359-8368(02)00012-4.

[6] Montazeri A, Javadpour J, Khavandi A, Tcharkhtchi A, Mohajeri A. Mechanical properties of multi-walled carbon nanotube/epoxy composites. Mater Des 2010;31:4202–8. https://doi.org/10.1016/j.matdes.2010.04.018.

[7] Huang ZM, Zhang YZ, Kotaki M, Ramakrishna S. A review on polymer nanofibers by electrospinning and their applications in nanocomposites. Compos Sci Technol 2003;63:2223–53. https://doi.org/10.1016/S0266-3538(03)00178-7.

[8] Moniruzzaman M, Winey KI. Polymer nanocomposites containing carbon nanotubes. Macromolecules 2006;39:5194–205. https://doi.org/10.1021/ma060733p.

[9] Cha J, Jun GH, Park JK, Kim JC, Ryu HJ, Hong SH. Improvement of modulus, strength and fracture toughness of CNT/Epoxy nanocomposites through the functionalization of carbon nanotubes. Compos Part B Eng 2017;129:169–79. https://doi.org/10.1016/j.compositesb.2017.07.070.

[10] Goh PS, Ismail AF, Ng BC. Directional alignment of carbon nanotubes in polymer matrices: Contemporary approaches and future advances. Compos Part A Appl Sci Manuf 2014;56:103–26. https://doi.org/10.1016/j.compositesa.2013.10.001.

[11] Ajayan BPM, Schadler LS, Giannaris C, Rubio A. Single-walled carbon nanotube - polymer composites : strength and weakness **. Adv Mater 2000;12:750–3.

[12] Esawi AMK, Farag MM. Carbon nanotube reinforced composites: potential and current challenges. Mater Des 2007;28:2394–401. https://doi.org/10.1016/j.matdes.2006.09.022.

[13] Gao L, Zhang Z, Thostenson ET, Byun J-H, Chou T-W. An assessment of the science and technology of carbon nanotube-based fibers and composites. Compos Sci Technol 2009;70:1–19. https://doi.org/10.1016/j.compscitech.2009.10.004.

[14] Gupta P, Rajput M, Singla N, Kumar V, Lahiri D. Electric field and current assisted alignment of CNT inside polymer matrix and its effects on electrical and mechanical properties. Polym (United Kingdom) 2016;89:119–27. https://doi.org/10.1016/j.polymer.2016.02.025.

[15] Fischer JE, Zhou W, Vavro J, Llaguno MC, Guthy C, Haggenmueller R, et al. Magnetically aligned single wall carbon nanotube films: Preferred orientation and anisotropic transport properties. J Appl Phys 2003;93:2157–63. https://doi.org/10.1063/1.1536733.

[16] Ladani RB, Wu S, Kinloch AJ, Ghorbani K, Zhang J, Mouritz AP, et al. Multifunctional properties of epoxy nanocomposites reinforced by aligned nanoscale carbon. Mater Des 2016;94:554–64. https://doi.org/10.1016/j.matdes.2016.01.052.

[17] Greenhall J, Homel LJ, Raeymaekers B. Ultrasound directed self-assembly processing of nanocomposites with ultra-high carbon nanotube weight fractions. J Compos Mater 2018;53. https://doi.org/10.1177/0021998318801452.

[18] Ma C, Liu HY, Du X, Mach L, Xu F, Mai YW. Fracture resistance, thermal and electrical properties of epoxy composites containing aligned carbon nanotubes by low magnetic field. Compos Sci Technol 2015;114:126–35. https://doi.org/10.1016/j.compscitech.2015.04.007.

[19] Wu S, Ladani RB, Ravindran AR, Zhang J, Mouritz AP, Kinloch AJ, et al. Aligning carbon nanofibres in glass-fibre/epoxy composites to improve interlaminar toughness and crack-detection capability. Compos Sci Technol 2017;152:46–56. https://doi.org/10.1016/j.compscitech.2017.09.007.

[20] Martin JJ, Fiore BE, Erb RM. Designing bioinspired composite reinforcement architectures via 3D magnetic printing. Nat Commun 2015;6. https://doi.org/10.1038/ncomms9641.

[21] Thostenson ET, Chou T. Aligned multi-walled carbon nanotube-reinforced composites : processing and mechanical characterization. J Phys D Appl Phys 2002;35. https://doi.org/10.1088/0022-3727/35/16/103.

[22] Llewellyn-Jones TM, Drinkwater BW, Trask RS. 3-D printed composites with ultrasonically arranged complex microstructure. Smart Mater Struct 2016;25. https://doi.org/10.1117/12.2218855.

[23] Oppenheim IJ, Whittaker MA, Dauson ER, Heard RA, Parra-Raad JA. Ultrasonic alignment of microparticles in nozzle-like geometries. Behav Mech Multifunct Mater Compos XII 2018;10596:28. https://doi.org/10.1117/12.2296868.

[24] Chavez LA, Regis JE, Delfin LC, Garcia Rosales CA, Kim H, Love N, et al. Electrical and mechanical tuning of 3D printed photopolymer–MWCNT nanocomposites through in situ dispersion. J Appl Polym Sci 2019;136. https://doi.org/10.1002/app.47600.

[25] Sharma A, Tripathi B, Vijay YK. Dramatic Improvement in properties of magnetically aligned CNT/polymer nanocomposites. J Memb Sci 2010;361:89–95. https://doi.org/10.1016/j.memsci.2010.06.005.

[26] Kamat PV, Thomas KG, Barazzouk S, Girishkumar G, Vinodgopal K, Meisel D. Self-assembled linear bundles of single wall carbon nanotubes and their alignment and deposition as a film in a dc field. J Am Chem Soc 2004;126:10757–62. https://doi.org/10.1021/ja0479888.

[27] Tanimoto Y, Fujiwara M, Shimomura Y, Mukouda I, Oki E, Hamada M. Magnetic Orientation and Magnetic Properties of a Single Carbon Nanotube. J Phys Chem A 2002;105:4383–6. https://doi.org/10.1021/jp004620y.

[28] Kinsler LE, Frey AR, Coppens AB, Sanders JV. Fundamentals of acoustics. New York: John Wiley; 2000.

[29] Gor'kov LP. On the forces acting on a small particle in an acoustical field in an ideal fluid. Sov Phys Dokl 1962;6:773.

[30] Collino RR, Ray TR, Fleming RC, Sasaki CH, Haj-Hariri H, Begley MR. Acoustic field controlled patterning and assembly of anisotropic particles. Extrem Mech Lett 2015;5:37–46. https://doi.org/10.1016/j.eml.2015.09.003.

[31] Greenhall J, Raeymaekers B. 3D printing macroscale engineered materials using ultrasound directed self-assembly and stereolithography. Adv Mater Technol 2017;2.. https://doi.org/10.1002/admt.201700122.

[32] Scholz MS, Drinkwater BW, Trask RS. Ultrasonic assembly of anisotropic short fibre reinforced composites. Ultrasonics 2014;54:1015–9. https://doi.org/10.1016/j.ultras.2013.12.001.

[33] Haslam MD, Raeymaekers B. Aligning carbon nanotubes using bulk acoustic waves to reinforce polymer composites. Compos Part B Eng 2014;60:91–7. https://doi.org/10.1016/j.compositesb.2013.12.027.

[34] Postiglione G, Natale G, Griffini G, Levi M, Turri S. Conductive 3D microstructures by direct 3D printing of polymer/carbon nanotube nanocomposites via liquid deposition modeling. Compos Part A Appl Sci Manuf 2015;76:110–4. https://doi.org/10.1016/j.compositesa.2015.05.014.

[35] Chapkin WA, McNerny DQ, Aldridge MF, He Y, Wang W, Kieffer J, et al. Real-time assessment of carbon nanotube alignment in a polymer matrix under an applied electric field via polarized Raman spectroscopy. Polym Test 2016;56:29–35. https://doi.org/10.1016/j.polymertesting.2016.09.018.

[36] Chapkin WA, Wenderott JK, Green PF, Taub AI. Length dependence of electrostatically induced carbon nanotube alignment. Carbon NY 2018;131:275–82. https://doi.org/10.1016/j.carbon.2018.01.014.

[37] Ayres CE, Jha BS, Meredith H, Bowman JR, Bowlin GL, Henderson SC, et al. Measuring fiber alignment in electrospun scaffolds : a user ' s guide to the 2D fast Fourier transform approach. J Biomater Sci Polym Edn 2008;19:603–21.

[38] Prisbrey M, Greenhall J, Guevara Vasquez F, Raeymaekers B. Ultrasound directed

self-assembly of three-dimensional user-specified patterns of particles in a fluid medium. J Appl Phys 2017;121. https://doi.org/10.1063/1.4973190.

[39] Greenhall J, Guevara Vasquez F, Raeymaekers B. Continuous and unconstrained manipulation of micro-particles using phase-control of bulk acoustic waves. Appl Phys Lett 2013;103. https://doi.org/10.1063/1.4819031.

[40] King LV. On the acoustic radiation pressure on spheres. Proc R Soc A Math Phys Eng Sci 1934;147:212–40. https://doi.org/10.1098/rspa.1934.0215.

[41] Sonin AA. A generalization of the Pi-theorem and dimensional analysis. Proc Natl Acad Sci USA 2004;101:8525–6. https://doi.org/10.1073/pnas.0402931101.

[42] Sen A, Srivastava M. Regression analysis: theory, methods and applications. New York: Springer-Verlag; 1990.

[43] Ladani RB, Wu S, Kinloch AJ, Ghorbani K, Zhang J, Mauritz AP, et al. Improving the toughness and electrical conductivity of epoxy nanocomposites by using aligned carbon nanofibres. Compos Sci Technol 2015;117:146–58. https://doi.org/10.1016/j.compscitech.2015.06.006.